Dyes and Pigments 92 (2011) 766–777

Contents lists available at ScienceDirect

Dyes and Pigments

journal homepage: www.elsevier.com/locate/dyepig

N-Aryl stilbazolium dyes as sensitizers for solar cells

Octavia A. Blackburn [a], Benjamin J. Coe [a,*], Valentine Hahn [a], Madeleine Helliwell [a], James Raftery [a], Yien T. Ta [a], Laurence M. Peter [b], Hongxia Wang [b], Juan A. Anta [c], Elena Guillén [c]

[a] School of Chemistry, University of Manchester, Oxford Road, Manchester M13 9PL, UK
[b] Department of Chemistry, University of Bath, Bath BA2 5NB, UK
[c] Area de Quimica Fisica, Departamento de Sistemas Físicos, Químicos y Naturales, Universidad Pablo de Olavide, 41013 Sevilla, Spain

ARTICLE INFO

Article history:
Received 18 May 2011
Accepted 12 June 2011
Available online 6 August 2011

Keywords:
Stilbazolium salts
Dye sensitizers
Solar cells
UV-visible absorption spectroscopy
Electrochemistry
Density functional theory

ABSTRACT

Eight new *N*-arylstilbazolium chromophores with electron donating $-NR_2$ (R = Me or Ph) substituents have been synthesized via Knoevenagel condensations and isolated as their PF_6^- salts. These compounds have been characterized by using various techniques including ^1H NMR and IR spectroscopies and electrospray mass spectrometry. UV–vis absorption spectra recorded in acetonitrile are dominated by intense, low energy $\pi \rightarrow \pi^*$ intramolecular charge-transfer (ICT) bands, and replacing Me with Ph increases the ICT energies. Cyclic voltammetric studies show irreversible reduction processes, together with oxidation waves that are irreversible for R = Me, but reversible for R = Ph. Single crystal X-ray structures have been determined for three of the methyl ester-substituted stilbazolium salts and for the Cl^- salts of their picolinium precursors. Time-dependent density functional theory calculations afford reasonable predictions of ICT energies, but greater rigour is necessary for $-NPh_2$ derivatives. The four new acid-functionalized dyes give moderate sensitization efficiencies (*ca.* 0.2%) when using TiO_2-based photoanodes, with relatively higher values for R = Ph *vs* Me, while larger efficiencies (up to 0.8%) are achieved with ZnO substrates.

1. Introduction

Given the urgent need to develop clean and renewable energy sources, there is much current interest in using molecular dyes, especially transition metal complexes, as sensitizers in solar energy harvesting [1]. Traditional silicon solar cells, which rely on absorption of photons by a p–n semiconductor junction, require high purity materials. Newer inorganic thin film alternatives, such as cadmium telluride or copper indium gallium selenide, are based on toxic or rare elements. In a major breakthrough in 1991, O'Regan and Grätzel reported efficient photosensitization of a wide band-gap semiconductor by a trinuclear Ru^{II}-2,2′-bipyridyl-based dye [2]. The chromophoric properties of such complexes derive from intense, low energy metal-to-ligand charge-transfer transitions.

A dye-sensitized solar cell (DSSC) contains a nanoparticulate film of a wide band-gap semiconductor such as TiO_2, coated with a dye monolayer. Photoexcitation of the dye results in electron injection into the conduction band of the semiconductor, and the dye is then regenerated by a species in the electrolyte (usually an organic solvent containing the I^-/I_3^- couple). Driven largely by the desire to avoid the use of relatively expensive metals such as ruthenium, many recent studies have focused on using purely organic dyes in DSSCs [3]. Although such an approach initially proved somewhat less effective when compared with using metal-based dyes, state-of-the-art organic sensitizers are now becoming competitive [4].

Motivated by potential applications in the field of nonlinear optics, we have investigated previously a range of stilbazolium dyes that contain *N*-arylpyridinium groups which act as strong electron acceptors [5]. Although pyridinium groups are often exploited in nonlinear optical chromophores [6], and also as electron acceptors in other photo-active molecular assemblies [7], we are not aware of any instances in which such substituents have been used in dyes for solar cell applications. Since they are much stronger electron acceptors than the carboxylate group which is typically found in dye sensitizers, strongly red-shifted $\pi \rightarrow \pi^*$ intramolecular charge-transfer (ICT) bands may be anticipated; increased absorption into the red and NIR regions will improve matching with the AM 1.5 solar spectrum when compared with most existing sensitizers. In addition, the ICT absorptions of previously studied *N*-aryl-stilbazolium species are relatively intense (with molar extinction coefficients ε of up to *ca.* 75×10^3 M^{-1} cm^{-1}), fulfilling another of

* Corresponding author. Tel.: +44 161 275 4601; fax: +44 161 275 4598.
E-mail address: b.coe@manchester.ac.uk (B.J. Coe).

0143-7208/$ – see front matter © 2011 Elsevier Ltd. All rights reserved.
doi:10.1016/j.dyepig.2011.06.017

the key requirements for potentially efficient sensitization. This report concerns experimental and theoretical studies including four such new chromophores functionalized with ester groups which act as precursors to carboxylate units for anchoring to oxide surfaces.

2. Experimental

2.1. Materials and procedures

We have reported previously the synthesis of the precursor compound *N*-(2,4-dinitrophenyl)-4-picolinium chloride, [dnppic$^+$]Cl; this material is unstable in air and quickly forms a tar-like substance which may be converted into its PF_6^- salt for improved handling [5a]. Therefore, [dnppic$^+$]Cl was treated as a reactive intermediate in this study and used without purification for reactions with aniline derivatives. All other reagents were obtained commercially and used as supplied. Products were dried at room temperature in a vacuum desiccator ($CaSO_4$).

2.2. General physical measurements

^{1}H NMR spectra were recorded on a Bruker AV-400 spectrometer and all shifts are referenced to TMS. The fine splitting of pyridyl or phenyl ring AA′BB′ patterns is ignored and the signals are reported as simple doublets, with *J* values referring to the two most intense peaks. Elemental analyses were performed by the Microanalytical Laboratory, University of Manchester. IR spectroscopy was performed on solid samples using an Excalibur BioRad FT-IR spectrometer, and UV–vis spectra were obtained by using a Shimadzu UV-2401 PC spectrophotometer. Mass spectra were measured by using + electrospray on a Micromass Platform II spectrometer with acetonitrile as the solvent.

Cyclic voltammetric measurements were carried out with an Ivium CompactStat. An EG&G PAR K0264 single-compartment microcell was used with a silver/silver chloride reference electrode (3 M NaCl, saturated AgCl) separated by a salt bridge from a glassy carbon disk working electrode and Pt wire auxiliary electrode. Acetonitrile was freshly distilled (from CaH_2) and [NBu_4^n]PF_6, as supplied from Fluka, was used as the supporting electrolyte. Solutions containing *ca.* 10^{-3} M analyte (0.1 M electrolyte) were deaerated by purging with N_2. All $E_{1/2}$ values were calculated from $(E_{pa} + E_{pc})/2$ at a scan rate of 200 mV s^{-1}.

2.3. Synthesis

2.3.1. N-(3,5-Bismethoxycarbonylphenyl)-4-picolinium chloride, [(3,5-MC$_2$Ph)pic$^+$]Cl

A solution of 4-picoline (2.4 mL, 25 mmol) and 2,4-dinitrochlorobenzene (5.00 g, 25 mmol) in ethanol (25 mL) was heated under reflux for 2 h. After cooling to room temperature, diethyl ether was added and the black precipitate was filtered off, washed with diethyl ether and dried. The crude product was purified by precipitation from boiling ethanol/diethyl ether. The resulting gray solid was filtered off, washed with diethyl ether and dried to afford crude [dnppic$^+$]Cl (5.01 g). A portion of this material, assumed to be monohydrated (0.500 g, 1.59 mmol), and dimethoxy-5-aminoisophthalate (3.54 g, 16.9 mmol) were added to isopropanol (50 mL), and the suspension was heated at reflux for 72 h. After cooling to room temperature, a dark green/brown residue was filtered off. The yellow filtrate was evaporated to dryness, then dissolved in water (100 mL) and extracted with chloroform. The pale brown aqueous layer was reduced to dryness, giving the crude product (0.305 g). Purification was effected by column chromatography on silica gel eluting with 80:20 dichloromethane/methanol. The major colourless band (fluorescent under short-wave UV light) was collected and evaporated to dryness to afford a peach-coloured solid. Yield: 0.194 g (35%, based on [dnppic$^+$]Cl·H_2O; 23% based on 4-picoline). δ_H (400 MHz, CD_3OD) 9.15 (2 H, d, $J = 6.8$ Hz, C_5H_4N), 8.87 (1 H, t, $J = 1.5$ Hz, C_6H_3), 8.67 (2 H, d, $J = 1.5$ Hz, C_6H_3), 8.17 (2 H, d, $J = 6.3$ Hz, C_5H_4N), 4.02 (6 H, s, 2CO_2Me), 2.83 (3 H, s, Me). ν(C=O) 1734 s cm^{-1}. Anal. Calcd (%) for $C_{16}H_{16}ClNO_4 \cdot 1.3H_2O$: C, 55.67; H, 5.43; N, 4.06. Found: C, 55.56; H, 5.10; N, 3.88. *m*/*z*: 286 ([M − Cl]$^+$).

2.3.2. N-(4-Methoxycarbonylphenyl)-4-picolinium chloride, [(4-MCPh)pic$^+$]Cl

This compound was prepared and purified in a manner similar to [(3,5-MC$_2$Ph)pic$^+$]Cl·$1.3H_2O$ by using methyl-4-aminobenzoate (2.56 g, 16.9 mmol) in place of dimethoxy-5-aminoisophthalate (crude product = 0.246 g). The product was finally crystallized by diffusion of diethyl ether vapour into an ethanol solution. Yield: 63 mg (14%, based on [dnppic$^+$]Cl·H_2O; 9% based on 4-picoline). δ_H (400 MHz, CD_3OD) 9.13 (2 H, d, $J = 6.8$ Hz, C_5H_4N), 8.35 (2 H, d, $J = 8.8$ Hz, C_6H_4), 8.15 (2 H, d, $J = 6.3$ Hz, C_5H_4N), 7.97 (2 H, d, $J = 9.1$ Hz, C_6H_4), 3.99 (3 H, s, CO_2Me), 2.81 (3 H, s, Me). ν(C=O) 1717 s cm^{-1}. Anal. Calcd (%) for $C_{14}H_{14}ClNO_2 \cdot 0.8H_2O$: C, 60.46; H, 5.65; N, 5.04. Found: C, 60.31; H, 5.56; N, 5.12. *m*/*z*: 228 ([M − Cl]$^+$).

2.3.3. (E)-4′-(Dimethylamino)-N-(3,5-bismethoxycarbonylphenyl)-4-stilbazolium hexafluorophosphate, [**1**]PF_6

[(3,5-MC$_2$Ph)pic$^+$]Cl·$1.3H_2O$ (100 mg, 0.290 mmol), 4-(dimethylamino)benzaldehyde (102 mg, 0.684 mmol) and piperidine (4 drops) were added to methanol (20 mL) and the mixture was heated at reflux for 4 h. Addition of diethyl ether (200 mL) to the purple solution afforded a dark precipitate which was filtered off, washed with diethyl ether and dried. Data for crude chloride salt, [**1**]Cl: δ_H (400 MHz, CD_3OD) 8.86–8.84 (3 H, C_5H_4N + C_6H_3), 8.61 (2 H, d, $J = 1.5$ Hz, C_6H_3), 8.12 (2 H, d, $J = 7.1$ Hz, C_5H_4N), 8.02 (1H, d, $J = 15.6$ Hz, CH), 7.68 (2 H, d, $J = 9.1$ Hz, C_6H_4), 7.20 (1 H, d, $J = 15.9$ Hz, CH), 6.81 (2 H, d, $J = 9.1$ Hz, C_6H_4), 4.02 (6 H, s, 2CO_2Me), 3.10 (6 H, s, NMe_2). ν(C=O) 1721 s cm^{-1}. This material was dissolved in 1:1 water/methanol and aqueous NH_4PF_6 (1 M) was added to give a dark purple precipitate which was filtered off, washed with water and dried. Yield: 120 mg (72%). δ_H (400 MHz, CD_3COCD_3) 9.12 (2 H, d, $J = 7.1$ Hz, C_5H_4N), 8.79 (1 H, t, $J = 1.4$ Hz, C_6H_3), 8.70 (2 H, d, $J = 1.5$ Hz, C_6H_3), 8.31 (2 H, d, $J = 7.1$ Hz, C_5H_4N), 8.17 (1 H, d, $J = 15.9$ Hz, CH), 7.71 (2 H, d, $J = 9.1$ Hz, C_6H_4), 7.36 (1 H, d, $J = 16.1$ Hz, CH), 6.85 (2 H, d, $J = 9.1$ Hz, C_6H_4), 4.00 (6 H, s, 2CO_2Me), 3.12 (6 H, s, NMe_2). ν(C=O) 1726 s cm^{-1}. Anal. Calcd (%) for $C_{25}H_{25}F_6N_2O_4P \cdot 0.5H_2O$: C, 52.54; H, 4.59; N, 4.90. Found: C, 52.40; H, 4.48; N, 4.68. *m*/*z*: 417 ([M − PF_6]$^+$).

2.3.4. (E)-4′-(Diphenylamino)-N-(3,5-bismethoxycarbonylphenyl)-4-stilbazolium hexafluorophosphate, [**2**]PF_6

This compound was prepared in a manner similar to [**1**]PF_6 by using 4-(diphenylamino)benzaldehyde (187 mg, 0.684 mmol) in place of 4-(dimethylamino)benzaldehyde to give a dark red solid. Yield: 177 mg (88%). δ_H (400 MHz, CD_3COCD_3) 9.25 (2 H, d, $J = 7.1$ Hz, C_5H_4N), 8.81 (1 H, t, $J = 1.5$ Hz, C_6H_3), 8.73 (2 H, d, $J = 1.5$ Hz, C_6H_3), 8.45 (2 H, d, $J = 7.1$ Hz, C_5H_4N), 8.21 (1 H, d, $J = 16.1$ Hz, CH), 7.72 (2 H, d, $J = 8.8$ Hz, C_6H_4), 7.53 (1 H, d, $J = 16.1$ Hz, CH), 7.43–7.39 (4 H, Ph), 7.24–7.18 (6 H, Ph), 7.01 (2 H, d, $J = 8.8$ Hz, C_6H_4), 4.01 (6 H, s, 2CO_2Me). ν(C=O) 1730 s cm^{-1}. Anal. Calcd (%) for $C_{35}H_{29}N_2O_4PF_6 \cdot 0.25H_2O$: C, 60.83; H, 4.30; N, 4.05. Found: C, 60.85; H, 4.10; N, 4.00. *m*/*z*: 541 ([M − PF_6]$^+$). Data for crude chloride salt, [**2**]Cl: δ_H (400 MHz, CD_3OD) 8.98 (2 H, d, $J = 7.1$ Hz, C_5H_4N), 8.87 (1 H, t, $J = 1.5$ Hz, C_6H_3), 8.64 (2 H, d, $J = 1.5$ Hz, C_6H_3), 8.24 (2 H, d, $J = 7.1$ Hz, C_5H_4N), 8.04 (1 H, d, $J = 16.1$ Hz, CH), 7.67 (2 H, d, $J = 8.8$ Hz, C_6H_4), 7.39–7.33 (5 H,

Ph + CH), 7.20–7.14 (6 H, Ph), 7.00 (2 H, d, J = 8.8 Hz, C_6H_4), 4.02 (6 H, s, $2CO_2Me$). ν(C=O) 1721 s cm^{-1}.

2.3.5. (E)-4′-(Dimethylamino)-N-(4-methoxycarbonylphenyl)-4-stilbazolium hexafluorophosphate, [3]PF_6

This compound was prepared in a manner similar to [**1**]PF_6 by using 4-(dimethylamino)benzaldehyde (125 mg, 0.838 mmol) and [(4-MCPh)pic]Cl·0.8H_2O (100 mg, 0.360 mmol) in place of [(3,5-MC_2Ph)pic$^+$]Cl·1.3H_2O to give a dark purple solid. Yield: 109 mg (60%). δ_H (400 MHz, CD_3COCD_3) 9.05 (2 H, d, J = 7.1 Hz, C_5H_4N), 8.33 (2 H, d, J = 8.6 Hz, C_6H_4), 8.29 (2 H, d, J = 7.1 Hz, C_5H_4N), 8.15 (1 H, d, J = 15.9 Hz, CH), 8.07 (2 H, d, J = 8.8 Hz, C_6H_4), 7.70 (2 H, d, J = 8.8 Hz, C_6H_4), 7.35 (1 H, d, J = 16.1 Hz, CH), 6.85 (2 H, d, J = 9.1 Hz, C_6H_4), 3.97 (3 H, s, CO_2Me), 3.12 (6 H, s, NMe_2). ν(C=O) 1714 s cm^{-1}. Anal. Calcd (%) for $C_{23}H_{23}N_2O_2PF_6$: C, 54.77; H, 4.60; N, 5.55. Found: C, 54.84; H, 4.46; N, 5.37. m/z: 359 ([M − PF_6]$^+$). Data for crude chloride salt, [**3**]Cl: δ_H (400 MHz, CD_3OD) 8.83 (2 H, d, J = 7.1 Hz, C_5H_4N), 8.33 (2 H, d, J = 8.8 Hz, C_6H_4), 8.12 (2 H, d, J = 7.1 Hz, C_5H_4N), 8.02 (1 H, d, J = 15.9 Hz, CH), 7.90 (2 H, d, J = 8.8 Hz, C_6H_4), 7.68 (2 H, d, J = 9.1 Hz, C_6H_4), 7.20 (1 H, d, J = 15.9 Hz, CH), 6.82 (2 H, d, J = 9.1 Hz, C_6H_4), 3.98 (3 H, s, CO_2Me), 3.10 (6 H, s, NMe_2). ν(C=O) 1715 s cm^{-1}.

2.3.6. (E)-4′-(Diphenylamino)-N-(4-methoxycarbonylphenyl)-4-stilbazolium hexafluorophosphate, [4]PF_6

This compound was prepared in a manner similar to [**3**]PF_6 by using 4-(diphenylamino)benzaldehyde (228 mg, 0.834 mmol) in place of 4-(dimethylamino)benzaldehyde to give a dark red solid. Yield: 140 mg (62%). δ_H (400 MHz, CD_3COCD_3) 9.16 (2 H, d, J = 7.1 Hz, C_5H_4N), 8.41 (2 H, d, J = 7.1 Hz, C_5H_4N), 8.34 (2 H, d, J = 8.8 Hz, C_6H_4), 8.19 (1 H, d, J = 16.1 Hz, CH), 8.09 (2 H, d, J = 8.8 Hz, C_6H_4), 7.71 (2 H, d, J = 8.8 Hz, C_6H_4), 7.51 (1 H, d, J = 16.1 Hz, CH), 7.43–7.39 (4 H, Ph), 7.23–7.18 (6 H, Ph), 7.00 (2 H, d, J = 8.8 Hz, C_6H_4), 3.97 (3 H, s, CO_2Me). ν(C=O) 1715 s cm^{-1}. Anal. Calcd (%) for $C_{33}H_{27}N_2O_2PF_6$: C, 63.06; H, 4.33; N, 4.46. Found: C, 62.86; H, 4.18; N, 4.27. m/z: 484 ([M − PF_6]$^+$). Data for crude chloride salt, [**4**]Cl: δ_H (400 MHz, CD_3OD) 8.87 (2 H, d, J = 7.1 Hz, C_5H_4N), 8.34 (2 H, d, J = 8.8 Hz, C_6H_4), 8.24 (2 H, d, J = 7.1 Hz, C_5H_4N), 8.04 (1 H, d, J = 16.1 Hz, CH), 7.93 (2 H, d, J = 8.8 Hz, C_6H_4), 7.66 (2 H, d, J = 8.8 Hz, C_6H_4), 7.39–7.33 (5 H, CH + Ph), 7.20–7.15 (6 H, Ph), 7.00 (2 H, d, J = 8.8 Hz, C_6H_4), 3.99 (3 H, s, CO_2Me). ν(C=O) 1713 s cm^{-1}.

2.3.7. (E)-4′-(Dimethylamino)-N-(3,5-biscarboxyphenyl)-4-stilbazolium hexafluorophosphate, [5]PF_6

The crude chloride salt [**1**]Cl was prepared exactly as described above, then dissolved in methanol (5 mL) and aqueous NaOH (2%, 1 mL) was added. The mixture was stirred at room temperature for 7 h and then acidified with concentrated H_2SO_4 (5 drops). Aqueous NH_4PF_6 (1 M) was added and the flask was left in a refrigerator overnight. The dark purple precipitate was filtered off, washed with water and dried. Yield: 33 mg (21%). δ_H (400 MHz, CD_3COCD_3) 9.15 (2 H, d, J = 7.1 Hz, C_5H_4N), 8.86 (1 H, t, J = 1.4 Hz, C_6H_3), 8.69 (2 H, d, J = 1.3 Hz, C_6H_3), 8.32 (2 H, d, J = 6.8 Hz, C_5H_4N), 8.18 (1 H, d, J = 15.9 Hz, CH), 7.71 (2 H, d, J = 8.8 Hz, C_6H_4), 7.37 (1 H, d, J = 15.6 Hz, CH), 6.85 (2 H, d, J = 9.1 Hz, C_6H_4), 3.13 (6 H, s, NMe_2). ν(C=O) 1716 s cm^{-1}. Anal. Calcd (%) for $C_{23}H_{21}F_6N_2O_4P$: C, 51.69; H, 3.96; N, 5.24. Found: C, 51.36; H, 4.11; N, 5.11. m/z: 411 ([M − PF_6 + Na]$^+$), 389 ([M − PF_6]$^+$).

2.3.8. (E)-4′-(Diphenylamino)-N-(3,5-biscarboxyphenyl)-4-stilbazolium hexafluorophosphate, [6]PF_6

The crude chloride salt [**2**]Cl was prepared exactly as described above, then treated as for [**5**]PF_6 to give a dark red/purple solid. Purification was effected by reprecipitation from acetone/diethyl ether. Yield: 24 mg (12%). δ_H (400 MHz, CD_3COCD_3) 9.24 (2 H, d, J = 7.1 Hz, C_5H_4N), 8.84 (1 H, t, J = 1.5 Hz, C_6H_3), 8.69 (2 H, d, J = 1.5 Hz, C_6H_3), 8.42 (2 H, d, J = 7.1 Hz, C_5H_4N), 8.19 (1 H, d, J = 16.1 Hz, CH), 7.68 (2 H, d, J = 8.8 Hz, C_6H_4), 7.50 (1 H, d, J = 15.9 Hz, CH), 7.40–7.36 (4 H, Ph), 7.20–7.15 (6 H, Ph), 6.98 (2 H, d, J = 8.8 Hz, C_6H_4). ν(C=O) 1713 s cm^{-1}. Anal. Calcd (%) for $C_{33}H_{25}F_6N_2O_4P·2.3H_2O$: C, 56.62; H, 4.26; N, 4.00. Found: C, 56.62; H, 3.96; N, 3.80. m/z: 557 ([M − PF_6 + 2Na]$^+$), 535 ([M − PF_6 + Na]$^+$), 513 ([M − PF_6]$^+$).

2.3.9. (E)-4′-(Dimethylamino)-N-(4-carboxyphenyl)-4-stilbazolium hexafluorophosphate, [7]PF_6

The crude chloride salt [**3**]Cl was prepared exactly as described above, then treated as for [**5**]PF_6 to give a dark purple solid. Yield: 46 mg (26%). δ_H (400 MHz, CD_3COCD_3) 9.06 (2 H, d, J = 7.1 Hz, C_5H_4N), 8.35 (2 H, d, J = 8.8 Hz, C_6H_4), 8.29 (2 H, d, J = 7.3 Hz, C_5H_4N), 8.16 (1 H, d, J = 15.9 Hz, CH), 8.06 (2 H, d, J = 8.8 Hz, C_6H_4), 7.71 (2 H, d, J = 8.8 Hz, C_6H_4), 7.35 (1 H, d, J = 15.9 Hz, CH), 6.85 (2 H, d, J = 9.1 Hz, C_6H_4), 3.13 (6 H, s, NMe_2). ν(C=O) 1702 s cm^{-1}. Anal. Calcd (%) for $C_{22}H_{21}F_6N_2O_2P·0.5H_2O$: C, 52.91; H, 4.44; N, 5.61. Found: C, 52.84; H, 4.03; N, 5.48. m/z: 367 ([M − PF_6 + Na]$^+$), 345 ([M − PF_6]$^+$).

2.3.10. (E)-4′-(Diphenylamino)-N-(4-carboxyphenyl)-4-stilbazolium hexafluorophosphate, [8]PF_6

The crude chloride salt [**4**]Cl was prepared exactly as described above, then treated as for [**5**]PF_6 to give a dark red/purple solid. Purification was effected by reprecipitation from acetone/diethyl ether. Yield: 22 mg (10%). δ_H (400 MHz, CD_3COCD_3) 9.19 (2 H, d, J = 7.1 Hz, C_5H_4N), 8.43 (2 H, d, J = 7.2 Hz, C_5H_4N), 8.36 (2 H, d, J = 8.7 Hz, C_6H_4), 8.20 (1 H, d, J = 16.1 Hz, CH), 8.10 (2 H, d, J = 8.8 Hz, C_6H_4), 7.71 (2 H, d, J = 8.3 Hz, C_6H_4), 7.52 (1 H, d, J = 16.1 Hz, CH), 7.43–7.39 (4 H, Ph), 7.23–7.19 (6 H, Ph), 7.01 (2 H, d, J = 8.3 Hz, C_6H_4). ν(C=O) 1707 s cm^{-1}. Anal. Calcd (%) for $C_{32}H_{25}F_6N_2O_2P·0.7H_2O$: C, 61.29; H, 4.24; N, 4.47. Found: C, 61.34; H, 4.13; N, 4.49. m/z: 483 ([M − PF_6 + Na]$^+$), 469 ([M − PF_6]$^+$).

2.4. X-ray crystallographic studies

Crystals of the salts [(4-MCPh)pic$^+$]Cl and [(3,5-MC_2Ph)pic$^+$]Cl·EtOH were grown by vapour diffusion of diethyl ether into ethanol solutions, while those of [**1**]PF_6, [**2**]PF_6·MeCN, and [**4**]PF_6·MeCN were obtained similarly with acetonitrile solutions. Data were collected on a Bruker APEX CCD X-ray diffractometer by using MoK_α radiation (λ = 0.71073 Å), and the data were processed by using the Bruker SAINT and SADABS [8] software packages. The structures were solved by direct methods using SHELXS-97 [9], and refined by full-matrix least-squares on all F_0^2 data using SHELXL-97 [10]. All non-hydrogen atoms were refined anisotropically and hydrogen atoms were included in idealized positions using the riding model, with thermal parameters of 1.2 times those of aromatic parent carbon atoms, and 1.5 times those of methyl parent carbons. The crystal of [(4-MCPh)pic$^+$]Cl was a weakly diffracting needle, so the data were cut at 0.9 Å resolution. The asymmetric unit of [**1**]PF_6 contains two cations and two PF_6^- anions with a disordered solvent fragment that could not be identified, but is presumably diethyl ether; all atoms of this group were defined as C at 0.5 occupancy and refined isotropically. For this structure, the phenyl rings were constrained to be regular hexagons, and restraints were also applied to the geometry of the pyridyl group. The crystal was very weakly diffracting and so the data were cut at 1.2 Å resolution. The crystals of [**4**]PF_6·MeCN were also extremely weakly diffracting, so the data were cut at 1 Å resolution. In this case, the asymmetric unit contains two cations, two PF_6^- anions and two acetonitrile molecules. The atoms C36–C53 are disordered over two sites, and the two components

of the disordered phenyl group were constrained to be regular hexagons. All other calculations were carried out by using the SHELXTL package [11]. Crystallographic data and refinement details are presented in Table 1.

The CCDC depositions 809 929 ([(4-MCPh)pic$^+$]Cl), 809 930 ([(3,5-MC$_2$Ph)pic$^+$]Cl·EtOH), 809 931 ([**1**]PF$_6$), 809 932 ([**2**]PF$_6$·MeCN) and 809 933 ([**4**]PF$_6$·MeCN) contain the supplementary crystallographic data for this paper. These data can be obtained free of charge via www.ccdc.cam.ac.uk/data_request/cif, data_request@ccdc.cam.ac.uk, or by contacting The Cambridge Crystallographic Data Centre, 12, Union Road, Cambridge CB2 1EZ, UK; fax: +44 1223 336033.

2.5. Theoretical calculations

Structure optimizations (B3LYP/6-311g*) [12,13] and time-dependent density functional theory calculations were carried out by using the Gaussian 03 software package [14]. The first 50 excited states were calculated in each case. The conductor-like polarizable continuum model (CPCM) [15] was employed to take account of the effect of acetonitrile on chromophore **6**. When using the crystal structure geometry, all counterions and solvent molecules were removed and methyl groups (on the esters) were replaced with protons (bond distance between O and H modified to 1.00 Å). The UV–vis absorption spectra were simulated by using the GaussSum program [16].

2.6. Fabrication of dye-sensitized solar cells

TiO$_2$-based cells were fabricated as follows. Fluorine-doped tin oxide (FTO) glass (TEC15, Hartford Glass) was cleaned by successive sonication for 15 min in aqueous detergent, acetone, isopropanol and ethanol. A thin compact layer (60 nm) of TiO$_2$ was then deposited on the cleaned FTO by spray pyrolysis. The mesoporous layers were prepared by doctor-blading a commercial TiO$_2$ paste (Dyesol, DSL-18-NR) onto the coated FTO substrates. The film was dried at 80 °C on a hotplate for 15 min and then sintered at 500 °C for 30 min to burn out the organic binder, leaving the mesoporous anatase structure of thickness around 13 μm. After cooling to about 100 °C, the films were immersed into 5×10^{-4} M solutions of the test dyes in acetonitrile and left for 16 h. Chenodeoxycholic acid (10^{-3} M) was added to the dye bath to reduce dye aggregation on the TiO$_2$ film. The dye-coated film was washed thoroughly with HPLC grade acetonitrile and then dried under nitrogen. The cells were assembled by sealing the dye-coated electrodes to thermally platinized FTO (TEC8) counter electrodes using a 25 μm thermoplastic gasket (Surlyn) at 80 °C under pressure. The narrow gap between the two electrodes was vacuum filled with electrolyte via holes predrilled in the counter electrode. The filling holes were sealed with a microscope slip by using Surlyn. The active area of the cells was 1.0 cm^2.

Two types of electrolyte were used in the TiO$_2$-based cells. Electrolyte A was composed of 0.06 M I$_2$, 0.6 M 1-propyl-3-methylimidiazoline iodide (PMII, Merck), 0.2 M NaI, 0.1 M guanidinium thiocyanate (GuSCN) and 0.5 M *tert*-butylpyridine (TBP) in 3-methoxypropionitrile (MPN). Electrolyte B (sodium-free) was composed of 0.03 M I$_2$, 0.6 M PMII, 0.1 M GuSCN and 0.5 M TBP in acetonitrile/valeronitrile (85:15 v/v). All of the chemicals used in the cell fabrication were obtained from Sigma–Aldrich unless stated otherwise.

ZnO-based cells were fabricated as follows. The ZnO paste was prepared by using a 1:1 mixture of two commercial ZnO powders, Evonik VP AdNano@ZnO20 (particle size *ca.* 20 nm) and PI-KEM (particle size *ca.* 50 nm). For thin film preparation the mixture was dispersed in water and ethanol (30:70) and stirred overnight to obtain a colloidal suspension of 30 wt%. This suspension was spread onto previously cleaned FTO glass with a glass rod using Scotch tape as spacer, and the film was then heated at 420 °C for 30 min. The ZnO substrates were coated with the test dyes in similar manner to the TiO$_2$ films, but using an immersion time of only 30 min. A photoanode coated with the reference dye D149 (Mitsubishi Paper Mills Limited) was prepared similarly, but using 7×10^{-4} M chenodeoxycholic acid in *tert*-butyl alcohol/acetonitrile (1:1). The counter electrode was prepared by spreading 15 μl of *platisol* (Solaronix) on the conductive side of TEC8 electrodes and subsequent annealing at 400 °C for 5 min. Cells with an active area

Table 1
Crystallographic data and refinement details for the salts [(4-MCPh)pic$^+$]Cl, [(3,5-MC$_2$Ph)pic$^+$]Cl·EtOH, [**1**]PF$_6$, [**2**]PF$_6$·MeCN and [**4**]PF$_6$·MeCN.

	[(4-MCPh)pic$^+$]Cl	[(3,5-MC$_2$Ph)pic$^+$]Cl·EtOH	[**1**]PF$_6$	[**2**]PF$_6$·MeCN	[**4**]PF$_6$·MeCN
formula	$C_{14}H_{14}ClNO_2$	$C_{18}H_{22}ClNO_5$	$C_{56}H_{50}F_{12}N_4O_8P_2$	$C_{37}H_{32}F_6N_3O_4P$	$C_{35}H_{30}F_6N_3O_2P$
M_W	263.71	367.82	1196.94	727.63	669.59
cryst syst	orthorhombic	monoclinic	triclinic	triclinic	triclinic
space group	*Fdd*2	*P*2/c	$P\bar{1}$	$P\bar{1}$	$P\bar{1}$
a (Å)	28.673(15)	12.232(2)	6.914(9)	8.0011(16)	9.832(7)
b (Å)	42.40(2)	6.7253(12)	11.460(14)	10.175(2)	10.682(7)
c (Å)	4.232(2)	23.092(4)	17.32(2)	21.333(4)	29.87(2)
α (deg)	90	90	84.56(2)	99.113(4)	81.414(13)
β (deg)	90	102.791(3)	84.58(2)	95.656(4)	86.504(13)
γ (deg)	90	90	87.50(2)	96.570(3)	76.879(12)
U (Å^3)	5145(5)	1852.6(6)	1359(3)	1691.4(6)	3020(4)
Z	16	4	1	2	4
D_{calcd} (Mg m^{-3})	1.362	1.319	1.463	1.429	1.473
T (K)	100(2)	100(2)	100(2)	100(2)	100(2)
μ (mm^{-1})	0.290	0.233	0.180	0.160	0.167
crystal size (mm)	0.80 × 0.02 × 0.02	0.33 × 0.30 × 0.25	0.60 × 0.10 × 0.05	0.75 × 0.15 × 0.05	0.60 × 0.10 × 0.04
crystal appearance	colourless needle	orange block	red plate	red plate	red plate
no. of reflns collected	7750	13 878	3952	10 448	10 926
no. of independent reflns (R_{int})	1844 (0.1909)	3774 (0.0835)	1650 (0.1961)	4838 (0.0596)	6256 (0.1265)
θ_{max} (deg) (completeness)	23.25 (99.9%)	25.00 (99.7%)	17.22 (99.9%)	23.26 (99.7%)	20.81 (98.9%)
reflns with $I > 2\sigma(I)$	1127	2387	820	3850	2927
GOF on F^2	0.914	1.020	1.107	1.135	0.873
final *R*1, *wR*2 [$I > 2\sigma(I)$]	0.0762, 0.1286	0.0695, 0.1313	0.1434, 0.3187	0.0713, 0.1443	0.0700, 0.0947
(all data)	0.1278, 0.1468	0.1169, 0.1481	0.2254, 0.3658	0.0925, 0.1534	0.1586, 0.1158
peak and hole (eÅ^{-3})	0.340, −0.277	0.678, −0.880	0.675, −0.334	0.951, −0.412	0.294, −0.309

of 0.81 cm^2 were assembled exactly as those containing the TiO_2 films.

Five different electrolyte solutions were tested in the ZnO-based cells with the dye salt [**7**]PF_6: (1) 0.5 M LiI, 0.05 M I_2, 0.5 M TBP in MPN; (2) 5×10^{-5} M I_2, 0.5 M TBAI in acetonitrile/ethylene carbonate (1:4); (3) 0.5 M LiI, 0.03 M I_2, 0.5 M TBP, 0.1 M GuSCN in acetonitrile; (4) 0.03 M I_2, 0.6 M PMII, 0.1 M GuSCN, 0.5 M TBP in acetonitrile; (5) 0.06 M I_2, 0.6 M PMII, 0.2 M NaI, 0.1 M GuSCN, 0.5 M TBP in MPN. Electrolyte 2 gave the best cell performance, so data were obtained for [**8**]PF_6 in only this electrolyte.

2.7. Current–voltage measurements

The current–voltage characteristics of the TiO_2-based cells were measured by using a solar simulator (Müller) equipped with 1 kW xenon lamp. The intensity of the illumination was calibrated with a standard silicon reference cell (Fraunhofer ISE) to provide 1 sun (100 mW cm^{-2}). AM 1.5 and KG5 filters were used to minimize the mismatch between the solar simulator and the AM 1.5 solar spectrum. The current–voltage plots were recorded by using a computer-controlled system (Whistonbrook).

The ZnO-based cells were characterized with a solar simulator (ABET) combined with a AM 1.5G filter. A reference cell with temperature output (Oriel, 91 150) was used to calibrate the illumination output to 1 sun. Photocurrents, photovoltages and current–voltage curves were measured by using a 2400 Keithley SourceMeter.

2.8. Incident-photon-to-electron conversion efficiency (IPCE) measurements

The IPCE of the TiO_2-based cells was measured with a home-made setup. Illumination was provided by a tungsten lamp in combination with a monochromator (Bentham, England). A yellow filter was employed at wavelengths above 550 nm to eliminate second-order diffracted light, and no bias illumination was used. The photon flux at each wavelength was measured by a calibrated photodiode (SD-112 UV), and the photocurrent generated by the cell at each wavelength was recorded by a current amplifier and A/D converter (SR 850, Stanford Research System).

3. Results and discussion

3.1. Synthesis and characterization

We have investigated previously salts of *N*-arylstilbazolium cations as materials for nonlinear optics [5]. These studies confirm the strong electron-accepting nature of the pyridinium groups in such molecules, revealing intense ICT absorptions in the visible region that may be exploitable in DSSCs. The new cations **1**–**4** (Fig. 1) were synthesized by using an established method that involves Knoevenagel condensation of an aldehyde with a picolinium derivative. The required new chloride salt precursors [(3,5-MC_2Ph)pic$^+$]Cl and [(4-MCPh)pic$^+$]Cl were prepared via Zincke-type reactions with [dnppic$^+$]Cl [5a], and isolated in moderate yields after column chromatography on silica gel. Base-catalyzed ester hydrolysis of **1**–**4** affords the acid-functionalized dyes **5**–**8** (Fig. 1), albeit in low isolated yields (10–26%).

The IR spectra of the new compounds all show relatively intense ν(C=O) stretching bands, together with various other absorptions, most notably those due to the PF_6^- anions in [**1**–**8**]PF_6 (a very intense band due to a stretching mode at *ca.* 835–840 cm^{-1}, together with a sharper but somewhat less intense band at *ca.* 560 cm^{-1} due to a bending mode). The energies of the ν(C=O) bands show several general trends: (i) replacing R = Me with Ph has little effect; (ii) the disubstituted species always have higher ν(C=O) values (by 6–17 cm^{-1}) when compared with their mono-substituted analogues; (ii) ester hydrolysis lowers ν(C=O) by 8–17 cm^{-1}.

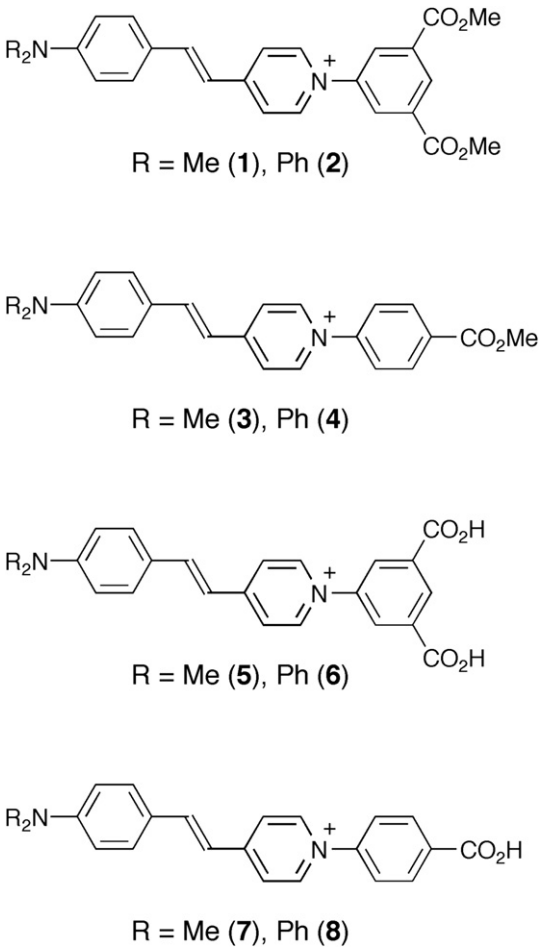

Fig. 1. Chemical structures of the stilbazolium cations investigated; all were isolated and studied as their PF_6^- salts.

3.2. Electronic absorption spectroscopy

UV–vis absorption data for [**1**–**8**]PF_6 in acetonitrile are presented in Table 2, and representative spectra of [**3**]PF_6 and [**4**]PF_6 are shown in Fig. 2. These spectra are dominated by intense ICT bands in the visible region, and also show one or more weaker bands due to $\pi \rightarrow \pi^*$ transitions having limited directional nature at higher energies.

In each case, replacing R = Me with Ph causes the ICT E_{max} value to increase by *ca.* 0.1 eV (Fig. 2). This trend reflects the weaker π-electron donating strength of the diarylamino group inferred by Kwon et al. by using density functional theory (DFT)-calculated bond distances and ^{13}C NMR chemical shifts [17]. The ICT band intensities show little sensitivity to R. The spectra are not affected significantly either by hydrolysis of the ester groups or by varying the substitution pattern on the phenyl ring attached to the pyridyl group.

3.3. Electrochemistry

Cyclic voltammetric data for [**1**–**8**]PF_6 in acetonitrile are presented in Table 2, and representative voltammograms of [**1**]PF_6 and

Table 2
UV–vis absorption and electrochemical data for salts [**1**–**8**]PF_6 in acetonitrile.

Salt	λ_{max}, nm (ε, 10^3 M^{-1} cm^{-1})[a]	E_{max}, eV[a]	Assignment	E, V *vs* Ag–AgCl (ΔE_p, mV)[b]		
				E_{pa}[c]	Oxidation $E_{1/2}$	Reduction[d]
[**1**]PF_6	276 (11.7)	4.49	$\pi \rightarrow \pi^*$	0.92		−0.79
	307 (10.7)	4.04	$\pi \rightarrow \pi^*$			
	518 (51.2)	2.39	ICT			
[**2**]PF_6	279sh (18.5)	4.44	$\pi \rightarrow \pi^*$	1.09	1.04 (100)	−0.74
	303 (23.2)	4.09	$\pi \rightarrow \pi^*$			
	502 (54.5)	2.47	ICT			
[**3**]PF_6	276 (12.7)	4.49	$\pi \rightarrow \pi^*$	0.92		−0.79
	310 (13.0)	4.00	$\pi \rightarrow \pi^*$			
	519 (54.9)	2.39	ICT			
[**4**]PF_6	279sh (20.1)	4.44	$\pi \rightarrow \pi^*$	1.09	1.04 (100)	−0.73
	305 (23.4)	4.07	$\pi \rightarrow \pi^*$			
	502 (53.6)	2.47	ICT			
[**5**]PF_6	276 (8.63)	4.49	$\pi \rightarrow \pi^*$	0.96		−0.80
	310 (9.21)	4.00	$\pi \rightarrow \pi^*$			
	516 (41.5)	2.40	ICT			
[**6**]PF_6	278sh (16.5)	4.46	$\pi \rightarrow \pi^*$	1.04	1.02 (60)	−0.71
	303 (22.0)	4.09	$\pi \rightarrow \pi^*$			
	500 (44.7)	2.48	ICT			
[**7**]PF_6	276 (8.54)	4.49	$\pi \rightarrow \pi^*$	0.93		−0.79
	310 (9.27)	4.00	$\pi \rightarrow \pi^*$			
	516 (44.5)	2.40	ICT			
[**8**]PF_6	278sh (16.8)	4.46	$\pi \rightarrow \pi^*$	1.08	1.04 (80)	−0.72
	304 (22.2)	4.08	$\pi \rightarrow \pi^*$			
	498 (41.9)	2.49	ICT			

[a] Solutions *ca.* 10^{-5} M.
[b] Solutions *ca.* 10^{-3} M in analyte and 0.1 M in [NBu^n_4]PF_6; potentials quoted for voltammograms recorded at a scan rate of 200 mV s^{-1} by using a glassy carbon working electrode. Ferrocene internal reference $E_{1/2}$ = 0.45 V, ΔE_p = 80 mV.
[c] For an irreversible process.
[d] E_{pc} for an irreversible process.

[**2**]PF_6 are shown in Fig. 3. Each compound shows a single process attributable to one-electron oxidation of the HOMO, presumably located primarily on the phenylamino unit, at *ca.* 1 V *vs* Ag–AgCl; these processes are irreversible when R = Me, but reversible when R = Ph (Fig. 3). This difference is likely attributable to delocalization, and hence stabilization, of the positive charge over the phenyl rings in the $-NPh_2$ derivatives. The E_{pa} values for the latter are always somewhat higher than those for their $-NMe_2$ analogues, in keeping with the stronger relative electron donating ability of the dimethylamino group (see above). In each case, an irreversible wave is also observed due to one-electron reduction of the LUMO,

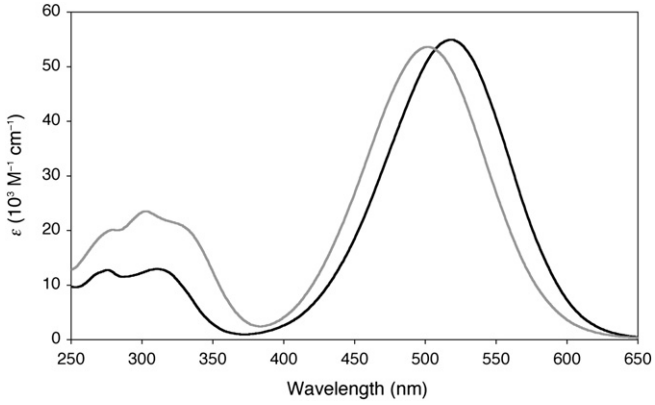

Fig. 2. UV–vis absorption spectra of [**3**]PF_6 (black) and [**4**]PF_6 (gray) at 293 K in acetonitrile.

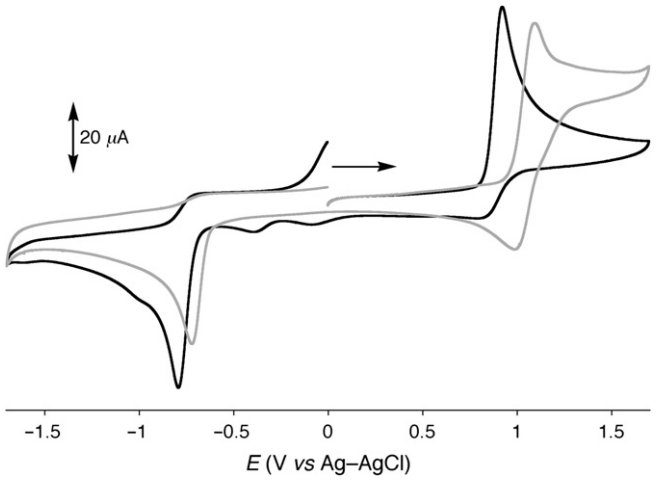

Fig. 3. Cyclic voltammograms for [**1**]PF_6 (black) and [**2**]PF_6 (gray) recorded at 200 mV s^{-1} in acetonitrile with a glassy carbon working electrode. The arrow indicates the direction of the initial scans.

presumably located largely on the pyridinium moiety, with $E_{pc} \approx -(0.7–0.8)$ V *vs* Ag–AgCl. Similar behaviour is found for related stilbazolium derivatives [5], and the irreversible nature of these processes is attributable to the presence of the ethenylene units which can engage readily in chemical reactions upon reduction. Small increases in E_{pc} (50–90 mV) on replacing Me with Ph in the new compounds show that the reduction occurs more readily when the weaker electron donor group is present, i.e., the LUMO becomes stabilized.

3.4. X-ray crystallography

Representations of the molecular structures of the salts [(4-MCPh)pic^+]Cl, [(3,5-MC_2Ph)pic^+]Cl·EtOH, [**1**]PF_6, [**2**]PF_6·MeCN and [**4**]PF_6·MeCN are shown in Figs. 4–8. These structures show geometric parameters that are generally similar to those found in related compounds [5], so detailed discussion is unnecessary. The respective dihedral angles between the pyridyl and phenyl ring in [(4-MCPh)pic^+]Cl and [(3,5-MC_2Ph)pic^+]Cl·EtOH are *ca.* 39.5° and 48.5°, while the corresponding twists in [**1**]PF_6, [**2**]PF_6·MeCN and [**4**]PF_6·MeCN are *ca.* 31.2°, 44.8° and 34.2/38.6° (two independent cations), respectively. As expected, the increased π-conjugation and lack of steric hindrance leads to smaller dihedral angles between the two aryl rings of the stilbazolium fragments; *ca.* 25.0°, 8.7° and 31.3/29.5° in [**1**]PF_6, [**2**]PF_6·MeCN and [**4**]PF_6·MeCN, respectively.

3.5. Theoretical studies

In order to rationalize the electronic structures and optical properties of the new chromophores, time-dependent DFT (TD-DFT) calculations were carried out by using Gaussian 03 [14].

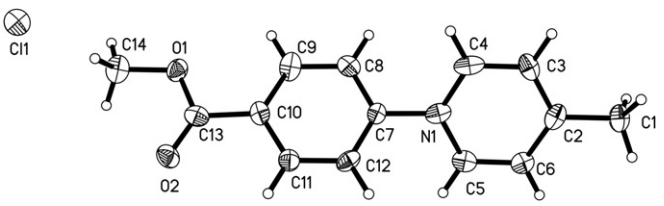

Fig. 4. Representation of the molecular structure of [(4-MCPh)pic^+]Cl (50% probability ellipsoids).

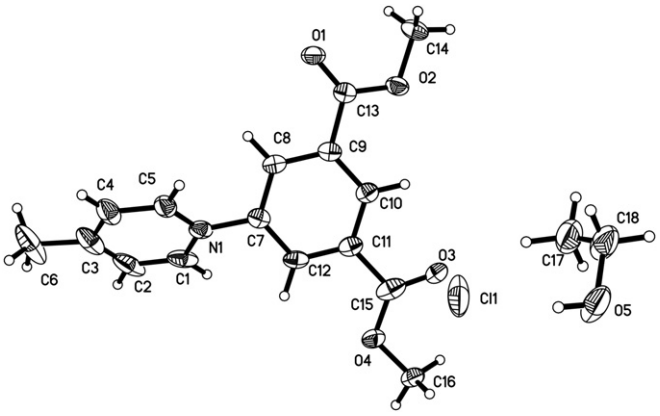

Fig. 5. Representation of the molecular structure of [(3,5-MC_2Ph)pic$^+$]Cl·EtOH (50% probability ellipsoids).

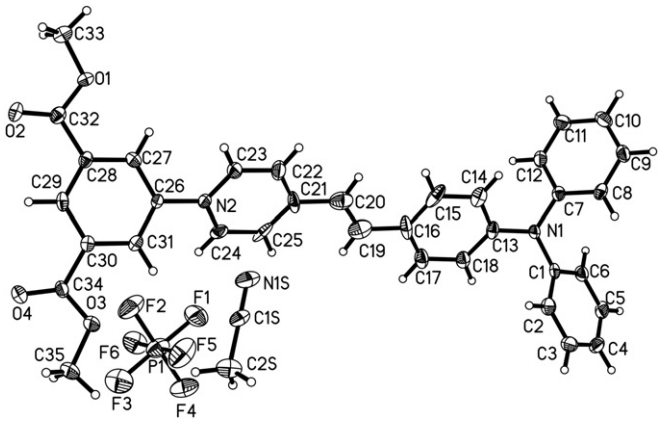

Fig. 7. Representation of the molecular structure of [**2**]PF_6·MeCN (50% probability ellipsoids).

The predicted transition energies and other details are presented in Table 3. The UV–vis spectra were simulated by using GaussSum [16], and selected spectra are shown in Figs. 9 and 10.

For the $-NMe_2$-substituted cation **5**, using the crystal structure geometry determined for the corresponding ester (in [**1**]PF_6, see above) gave an adequate fit with the observed UV–vis spectrum (Fig. 9). In the case of the related monosubstituted cation **7**, no directly relevant crystallographic data are available, so the structure was optimized before the TD-DFT calculations were carried out. For the $-NPh_2$-substituted chromophores, the calculations produced less consistent results. For **6**, using the crystal structure geometry determined for the corresponding ester (in [**2**]PF_6·MeCN, see above) gave a very poor fit with the observed UV–vis spectrum (Fig. 10a). Therefore, the structure was optimized and the TD-DFT calculations repeated, giving a better match between the predicted and observed spectra. Additional inclusion of an acetonitrile solvent continuum (CPCM) further improves the agreement with the experimental spectrum (Fig. 10b). In the case of **8**, using the crystallographic coordinates for [**4**]PF_6·MeCN also gave relatively inaccurate results, but geometry optimization has not been performed with this molecule. Optimization of **6** alters the geometry when compared with the related crystal structure. The stilbazole portion is flattened out slightly to become almost perfectly planar, while the dihedral angles between this fragment and the acid-substituted phenyl ring and between the *N*-phenyl and phenylene rings increase. Similar differences are evident between the crystallographic model and optimized structures of **7**.

In all cases, the lowest energy absorption band is confirmed to have ICT HOMO → LUMO character with a large transition dipole moment μ_{12}. Inspection of the frontier orbitals (Fig. 11) shows that the HOMOs reside mainly on the aminophenyl and ethenylene groups, with some contribution from the pyridyl rings. The LUMOs are spread across the whole molecule, but with major contributions from the pyridyl rings and ethenylene units. The higher energy band is in all cases calculated to be made up of two separate transitions, and the intensities of these relative to the main band vary somewhat. The ICT energies predicted via TD-DFT when using the crystal structure geometries are lower than the experimental values (Tables 2 and 3). Such differences are commonly found when using TD-DFT to model ICT transitions, as noted in other studies relevant to DSSCs [3c]. This underestimation of the excitation energy is reasonable for **5** (0.10 eV), but very large for **6** (0.81 eV) and **8** (0.78 eV). While structure optimization and inclusion of the CPCM for **6** produces a closer match between the calculated ΔE and the experimental E_{max} value, this energy is still underestimated by 0.19 eV. Studies by Liu et al. with arylfluorene derivatives having two $-NPh_2$ substituents underestimated ΔE to a similar extent (*ca.* 0.2–0.4 eV) at the B3LYP/6-31G(d) level of theory [18]. Such discrepancies may be attributable to a neglect of solvation effects, but other factors may also be important. In contrast, geometry optimization for **7** gives an *overestimation* of the excitation energy, with ΔE being larger than E_{max} by 0.16 eV.

3.6. Sensitized solar cell studies

The basic physics and chemistry of DSSCs have been reviewed elsewhere [1d,19,20], including the derivations of key expressions used here [1d].

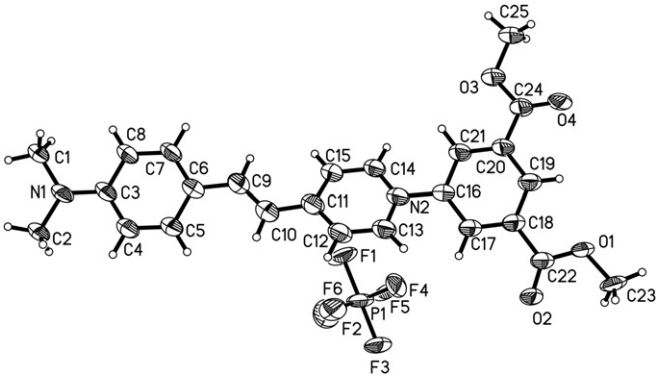

Fig. 6. Representation of the molecular structure of [**1**]PF_6 (50% probability ellipsoids).

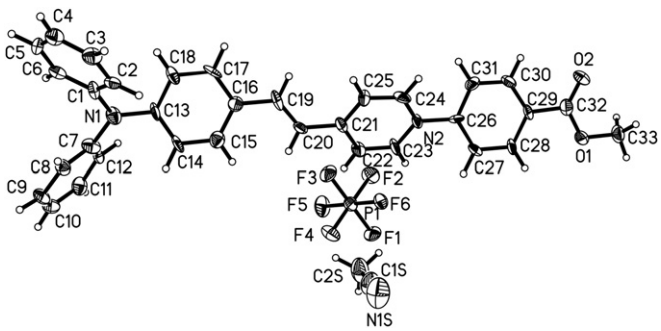

Fig. 8. Representation of the molecular structure of [**4**]PF_6·MeCN, excluding the disordered cation and associated PF_6^- and MeCN molecules (50% probability ellipsoids).

Table 3
Data from TD-DFT (B3LYP/6-311g*) calculations on the cations **5**–**8**.

Cation	ΔE (eV)	f_{os}	Major contributions	μ_{12} (D)
5[a]	2.30	1.14	HOMO → LUMO	11.44
	3.52	0.23	HOMO−2 → LUMO	4.17
			HOMO → LUMO+3	
	3.71	0.30	HOMO−2 → LUMO	4.63
			HOMO → LUMO+3	
			HOMO → LUMO+4	
6[a]	1.67	0.84	HOMO → LUMO	11.53
	3.07	0.23	HOMO−4 → LUMO	4.42
			HOMO → LUMO+3	
	3.14	0.40	HOMO−4 → LUMO	5.76
			HOMO → LUMO+3	
6[b]	2.20	1.41	HOMO → LUMO	12.99
	3.07	0.25	HOMO−1 → LUMO	4.63
	3.28	0.37	HOMO−3 → LUMO	5.49
6[c]	2.29	1.66	HOMO → LUMO	13.82
	3.42	0.34	HOMO−1 → LUMO	5.09
			HOMO → LUMO+2	
7[b]	2.56	1.59	HOMO → LUMO	12.78
	3.59	0.08	HOMO → LUMO+1	2.44
			HOMO → LUMO+2	
	3.82	0.20	HOMO−1 → LUMO	3.68
			HOMO → LUMO+4	
8[a]	1.71	0.85	HOMO → LUMO	11.47
	3.06	0.30	HOMO−3 → LUMO	5.09
			HOMO → LUMO+2	
	3.19	0.43	HOMO−4 → LUMO	5.98
			HOMO−3 → LUMO	
			HOMO → LUMO+2	

[a] Obtained by using the atomic coordinates from the X-ray crystal structure of the corresponding ester derivative.
[b] Obtained by using the atomic coordinates from the B3LYP/6-311g*-optimized structure.
[c] Obtained by using both the atomic coordinates from the B3LYP/6-311g*-optimized structure and the CPCM (acetonitrile).

The carboxylate-functionalized dye salts [**5**–**8**]PF_6 were tested initially in liquid electrolyte cells with mesoporous TiO_2 layers. Plots showing the *I*–*V* performance of these cells with electrolyte A are depicted in Fig. 12, and the AM 1.5 characteristics of the cells

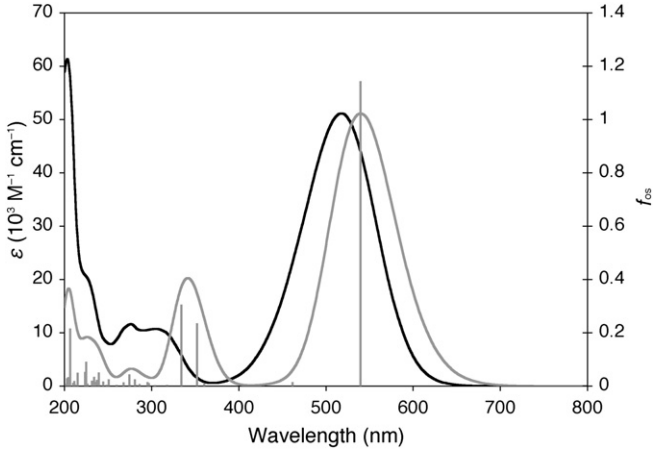

Fig. 9. TD-DFT-calculated (gray) and experimental (black) UV–vis spectra of chromophore **5** and [**5**]PF_6, the latter recorded in acetonitrile. The calculations used the crystal structure geometry determined for the corresponding ester (in [**1**]PF_6). The ε-axes refer to the experimental data only and the vertical axes of the calculated data are scaled to match the main experimental absorptions. The oscillator strength axes refer to the individual calculated transitions (vertical gray lines).

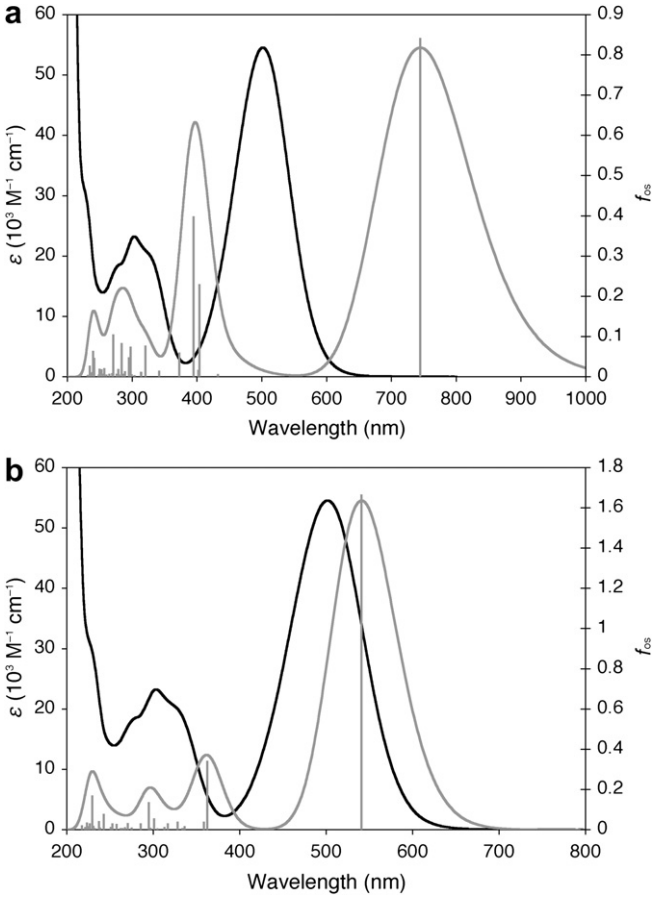

Fig. 10. TD-DFT-calculated (gray) and experimental (black) UV–vis spectra of **6** and [**6**]PF_6, the latter recorded in acetonitrile. The calculations used (a) the crystal structure geometry for the corresponding ester (in [**2**]PF_6·MeCN), and (b) the B3LYP/6-311g*-optimized structure with CPCM. All other details as for Fig. 9.

together with information on the LUMO energy levels of the dyes are summarized in Table 4.

The cells containing [**5**]PF_6, [**7**]PF_6 and [**8**]PF_6 give the same open-circuit voltage (V_{OC} = 467 mV), while [**6**]PF_6 gives a value higher by 26 mV (Table 4). The excess electron density $n_{light} - n_{dark}$ under illumination and hence the V_{OC} of a DSSC is determined by the balance between electron injection from the photoexcited sensitizer and back electron-transfer from the TiO_2 to the oxidized component of the I^-/I_3^- redox couple. For the usual case where $n_{light} >> n_{dark}$, the electron density under open-circuit conditions and first-order back electron-transfer is given by

$$n_{light} = \frac{\eta_{LH}\eta_{inj}I_0\tau}{d} \quad (1)$$

Here η_{LH} is the light harvesting efficiency (i.e., the fraction of incident photons absorbed), η_{inj} is the electron-injection efficiency, I_0 is the incident photon flux, τ is the lifetime of injected electrons and d is the thickness of the TiO_2 layer (τ corresponds to the inverse of the pseudo first-order rate constant for back electron-transfer to I_3^-). The V_{OC} value is determined by the ratio of electron concentrations under illumination and in the dark,

$$V_{OC} = \frac{k_B T}{q}\ln\frac{n_{light}}{n_{dark}} \quad (2a)$$

where n_{dark} is determined by the difference between the conduction band edge energy E_c and the redox Fermi level energy E_{Fn}.

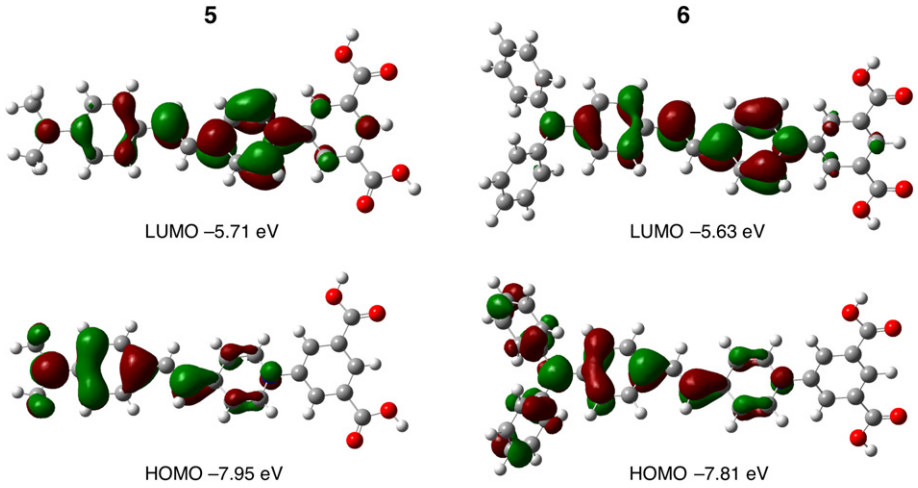

Fig. 11. TD-DFT-derived depictions of the main orbitals involved in the ICT transitions in **5** (using the X-ray crystal structure of the corresponding ester) and **6** (using the B3LYP/6-311g*-optimized structure) (isosurface value 0.03 au).

$$n_{\mathrm{dark}} = N_{\mathrm{c}} e^{-\left(\frac{E_{\mathrm{c}} - E_{\mathrm{Fn}}}{k_{\mathrm{B}} T}\right)} \tag{2b}$$

The higher V_{OC} for the cell sensitized with [**6**]PF_6 could be due to several different factors. Since η_{LH} and τ are expected to remain essentially constant for all four dyes, the most probable difference between them is either η_{inj} or the difference between E_c and E_{Fn}.

The second important characteristic of a DSSC is the short-circuit current density, J_{SC}. For AM 1.5 illumination, J_{SC} is determined by the product of the efficiencies for light harvesting, electron injection and electron collection (η_{col}). In principle, all three efficiencies may depend on photon energy, so that J_{SC} corresponds to the integral

$$J_{\mathrm{SC}} = q \int \eta_{\mathrm{LH}}(\lambda)\eta_{\mathrm{inj}}(\lambda)\eta_{\mathrm{col}}(\lambda) I(\lambda) \mathrm{d}\lambda \tag{3}$$

where q is the elementary charge. The J_{SC} values, which follow the sequence [**8**]PF_6 > [**6**]PF_6 >> [**7**]PF_6 = [**5**]PF_6 (Table 4, Fig. 12) are at least an order of magnitude lower than those measured for identical cells sensitized with the standard ruthenium complex N719 (J_{SC} = 11.4 mA cm^{-2}), so clearly electron losses are much higher with the new stilbazolium dyes. The electrolytes used here give η_{col} close to 100% with N719-based cells [21], so it is unlikely that collection losses explain the differences in J_{SC} in the present studies. All of the dyes [**5**–**8**]PF_6 absorb very strongly in the visible region, with ε values substantially higher than those of N719 and similar species (*ca.* 1.5–2 × 10^4 M^{-1} cm^{-1}). The red shifts of the ICT bands of the Me-substituted dyes with respect to their Ph analogues (Fig. 2) could lead to slightly higher η_{LH} values, so this factor cannot explain the higher J_{SC} values for [**6**]PF_6 and [**8**]PF_6. This leaves differences in the injection efficiencies, η_{inj} as the most likely explanation.

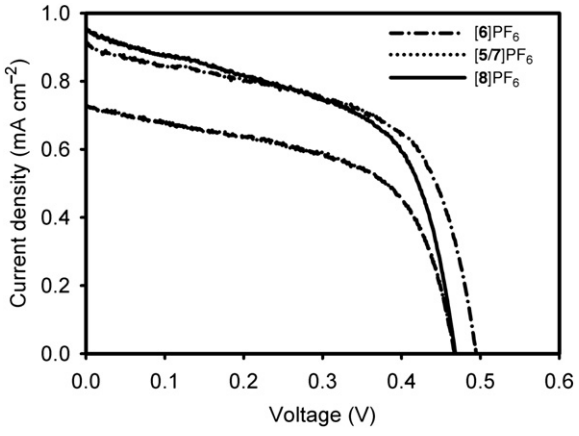

Fig. 12. AM 1.5 Current density-voltage characteristics of TiO_2-based DSSCs fabricated by using salts [**5**–**8**]PF_6 with electrolyte A.

The difference in performance of the dyes is also evident in the IPCE plots (Fig. 13). The highest IPCE is observed for the cell fabricated with [**8**]PF_6, and the lowest for that with [**5**]PF_6. The peak IPCE observed for [**8**]PF_6 is only *ca.* 9%, an order of magnitude lower than that for the best Ru-based sensitizers. These low IPCE values are consistent with the low J_{SC} values recorded for the cells.

In order to test whether poor injection is the cause of the low currents and voltages observed, the performance of cells sensitized with [**6**]PF_6 and filled with electrolytes A and B was compared. The results are shown in Fig. 14.

Substitution of electrolyte A (which contains Na^+) by the sodium-free electrolyte B lowers the J_{SC} values by a factor of 3, but increases V_{OC} by *ca.* 60 mV. The lower current and higher voltage in the sodium-free electrolyte can be attributed to upward movement of the TiO_2 conduction band relative to the I_3^-/I^- Fermi level. Alkali metal ions are known to lower the E_c of TiO_2 as a consequence of changing the surface dipole [22]. This sensitivity of the cell performance to electrolyte composition suggests that η_{inj} is influenced by the alignment of the excited state energy and E_c, but other factors may also be responsible for the low injection efficiencies.

Table 4
Current/voltage characteristics of TiO_2-based DSSCs containing [**5**–**8**]PF_6 with electrolyte A and the measured and calculated LUMO energies.

Salt	J_{SC} (mA cm^{-2})	V_{OC} (mV)	FF (%)	η (%)	LUMO (V)[a]	LUMO (eV)[b]
[**5**]PF_6	0.73	467	57	0.193	−0.80	−5.71
[**6**]PF_6	0.92	493	59	0.268	−0.71	−5.80
[**7**]PF_6	0.73	467	57	0.195	−0.79	−5.66
[**8**]PF_6	0.95	467	56	0.248	−0.72	−5.74

[a] Measured via cyclic voltammetry in acetonitrile (V *vs* Ag–AgCl).
[b] Obtained by using TD-DFT (B3LYP/6-311g*) calculations on the cation with the atomic coordinates from the X-ray crystal structure of the corresponding ester derivative, excepting **7** for which the B3LYP/6-311g*-optimized geometry was used.

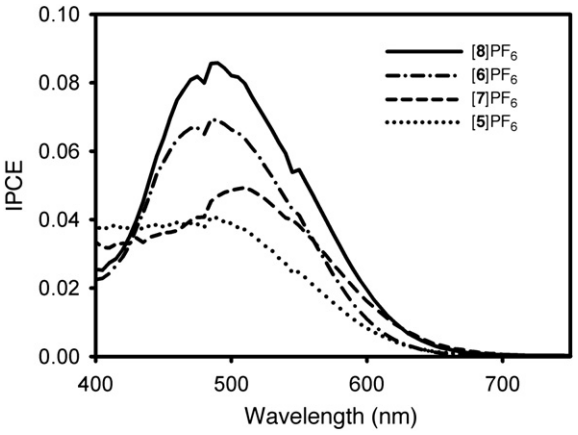

Fig. 13. IPCE plots for TiO_2-based DSSCs containing [**5**–**8**]PF_6.

While the data presented here do not relate to excited state properties, so provide only rough a guide, both the electrochemical measurements and the TD-DFT calculations (Table 4) indicate that the LUMO energies of the new dyes are too low with respect to the conduction band of TiO_2 to allow efficient electron injection. Experiments in acetonitrile-based electrolytes have yielded an E_c value of *ca.* −0.7 V *vs* Ag–AgCl [23], similar to or only a little higher than the potentials for reduction of the pyridinium groups in [**5**–**8**]PF_6. Furthermore, DFT calculations have been used to derive E_c values of *ca.* −(4–5) eV for TiO_2 nanoparticles [24], higher than our predicted LUMO energies. Our TD-DFT calculations also indicate that the LUMOs feature very little electron density on the acid-functionalized phenyl rings (Fig. 11). By contrast, the direct attachment of carboxylate groups to the electron-accepting 2,2′-bipyridyl ligands in Ru^{II}-based dyes gives a much more favourable electron density distribution in the excited states. Time-resolved studies of electron injection could give more information on this aspect of the sensitization process.

Although TiO_2 has been used most widely, various metal oxides can be used in DSSCs [1]. Therefore, we have also carried out studies with the representative dye salts [**7**]PF_6 and [**8**]PF_6 by using ZnO instead of TiO_2-based photoanodes, noting that the number of carboxylate substituents does not greatly affect the dye performance on the latter (Table 4). When compared with the TiO_2-based photoanodes, much shorter immersion times were used (30 min cf. 16 h). This change is intended to minimize chemical reactions between the dyes and ZnO, which is known to be unstable under both acidic and basic conditions [1f,25]. Five different electrolytes were tested with [**7**]PF_6, in order to find the most suitable. Dye desorption and thus a significant decrease of the photocurrent with time is observed for electrolytes 4 and 5. Desorption is also observed with electrolyte 6, although not as strongly as with 4 and 5. The data obtained by using electrolytes 1, 2 and 6 are shown in Table 5 and *I*–*V* curves are depicted in Fig. 15. Given that electrolyte 2 clearly gives the best performance, [**8**]PF_6 was also tested with this mixture. The *I*–*V* curves obtained under these conditions with [**7**]PF_6, [**8**]PF_6 or the indoline reference dye D149 [26] are shown in Fig. 16.

Table 5
Current/voltage characteristics of ZnO-based DSSCs containing [**7**]PF_6, [**8**]PF_6 or D149.

Dye	Electrolyte	J_{SC} (mA cm^{-2})	V_{OC} (mV)	FF (%)	η (%)
[**7**]PF_6	1	1.68	503	48	0.4
[**7**]PF_6	6	0.97	485	55	0.3
[**7**]PF_6	2	2.33	524	56	0.7
[**8**]PF_6	2	2.70	492	60	0.8
D149	2	8.38	668	35	2.0

Comparison with the data obtained when using TiO_2-based photoanodes (Table 4) shows that the overall efficiencies of solar cells sensitized with [**7**]PF_6 or [**8**]PF_6 are improved 3–4-fold by switching to ZnO. Since the E_c value of ZnO is more negative by *ca.* 100 mV when compared with that of TiO_2 (anatase) [27], this factor cannot be the cause of the increased performance of the new dyes with ZnO. However, electron injection depends also on other factors such as the local electric dipole at the surface and the dielectric constant of the oxide. It may be that the relatively higher electron mobility of ZnO which facilitates electron transport is also important, and/or recombination losses may be more significant in TiO_2. While the studies using both metal oxides show that the Ph-substituted dyes are more efficient than their Me analogues, the difference between [**7**]PF_6 and [**8**]PF_6 is less pronounced with ZnO.

The performance of the new dyes is still substantially below that of a common benchmark (in this case D149, Table 5), with J_{SC} values about 30% as large and V_{OC} values 143–176 mV lower. Nevertheless, these results are reasonably encouraging in the context of a first investigation with a new class of sensitizer molecule. In order to improve the performance of stilbazolium dyes, further tuning of both the energy levels and the electron donor-acceptor coupling will be necessary. One possibility that may be expected to affect

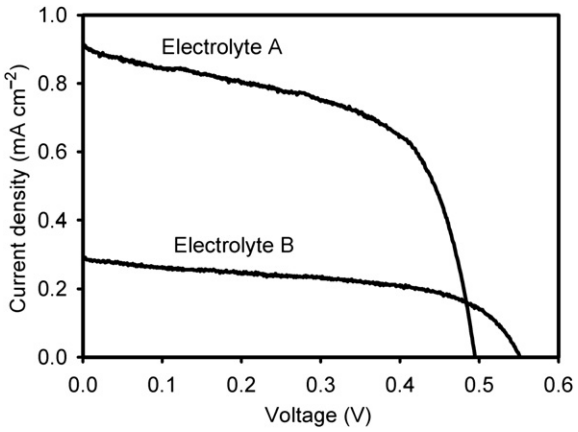

Fig. 14. AM 1.5 current–voltage characteristics of TiO_2-based DSSCs containing [**6**]PF_6 with electrolytes A and B.

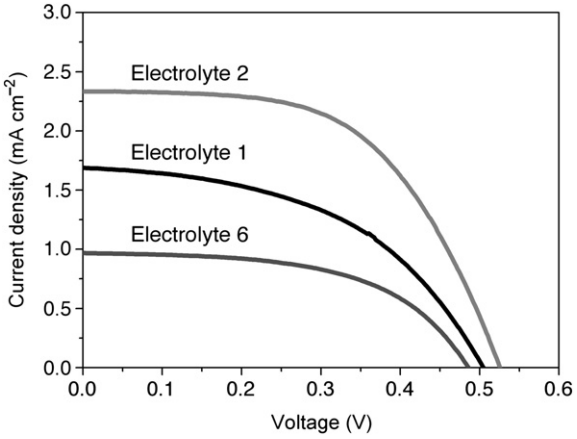

Fig. 15. AM 1.5 current–voltage characteristics of ZnO-based DSSCs containing [**7**]PF_6 with electrolytes 1, 2 and 6.

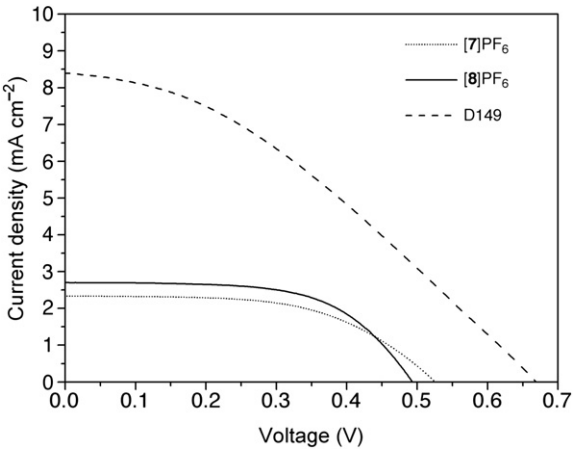

Fig. 16. AM 1.5 current–voltage characteristics of ZnO-based DSSCs containing electrolyte 2 and [**7**]PF_6, [**8**]PF_6 or D149.

both aspects beneficially is to use *N*-(2-carboxyvinyl)- instead of *N*-arylpyridinium groups.

4. Conclusions

We have synthesized and characterized a series of new PF_6^- salts of *N*-arylstilbazolium chromophores with $-NR_2$ (R = Me or Ph) substituents. Replacing Me with Ph causes blue shifts of the intense ICT absorption bands, due to the relatively weaker π-electron donating ability of the $-NPh_2$ group. In keeping with these observations, cyclic voltammetry shows that the $-NPh_2$ derivatives are oxidised less readily than their $-NMe_2$ analogues. These oxidation processes are irreversible when R = Me, but reversible when R = Ph. Irreversible waves at negative potentials are due to pyridinium reductions, with small increases in E_{pc} on replacing Me with Ph showing that the $-NPh_2$ derivatives are reduced more readily. Single crystal X-ray structures have been determined for three of the stilbazolium salts and also for the Cl^- salts of their picolinium precursors. TD-DFT calculations confirm the character of the visible absorptions, and predict the ICT energy reasonably accurately for a $-NMe_2$ derivative when using a crystallographically determined geometry. In contrast, for a $-NPh_2$ derivative, structure optimization and inclusion of an acetonitrile solvent continuum is necessary to avoid severe underestimation with respect to the measured ICT energy. DSSC studies with the new acid-functionalized compounds on TiO_2-based photoanodes afford moderate efficiencies of *ca.* 0.2%, with relatively higher values for R = Ph *vs* Me. When using ZnO substrates, larger sensitization efficiencies of up to 0.8% are achieved. The modest performance of these compounds is attributable to inefficient electron injection arising from thermodynamic and/or kinetic factors. However, considerable scope exists for future improvements in the sensitizing abilities of stilbazolium dyes via appropriate molecular engineering.

Acknowledgements

We thank the EPSRC for support in the form of a PhD studentship (YTT) and also DyStar UK Ltd and the University of Manchester for funding a PhD studentship (OAB). We are grateful to Dr Joseph J. W. McDouall (Manchester) for advice concerning TD-DFT calculations. The work in Bath was supported by the EPSRC (grant EP/E035469/1). EG and JAA thank the Ministerio de Ciencia e Innovación of Spain for project HOPE CSD2007-00007 (Consolider-Ingenio 2010), CTQ2009-10477 (TRANSLIGHT), and a FPU studentship, and Junta de Andalucia (Andalusian Regional Government) under projects P07-FQM-02595, P07-FQM-02600, and P09-FQM-04938.

References

[1] (a) Nazeeruddin MdK, Grätzel M. Conversion and storage of solar energy using dye-sensitized nanocrystalline TiO_2 cells. In: McCleverty JA, Meyer TJ, editors. Comprehensive coordination chemistry II, vol. 9. Oxford, UK: Pergamon Press; 2004. p. 719–58;
(b) Robertson N. Optimizing dyes for dye-sensitized solar cells. Angew Chem Int Ed 2006;45:2338–45;
(c) Durrant JR, Haque SA, Palomares E. Photochemical energy conversion: from molecular dyads to solar cells. Chem Commun; 2006:3279–89;
(d) Peter LM. Characterization and modeling of dye-sensitized solar cells. J Phys Chem C 2007;111:6601–12;
(e) Special issue on organic photovoltaics. Acc Chem Res 2009;42:1689–857;
(f) Hagfeldt A, Boschloo G, Sun L-C, Kloo L, Pettersson H. Dye-sensitized solar cells. Chem Rev 2010;110:6595–663.

[2] O'Regan B, Grätzel M. A low-cost, high-efficiency solar cell based on dye-sensitized colloidal TiO_2 films. Nature 1991;353:737–40.

[3] (a) Ning Z-J, Tian H. Triarylamine: a promising core unit for efficient photovoltaic materials. Chem Commun; 2009:5483–95;
(b) Mishra A, Fischer MKR, Bäuerle P. Metal-free organic dyes for dye-sensitized solar cells: from structure:property relationships to design rules. Angew Chem Int Ed 2009;48:2474–99;
(c) Pastore M, Mosconi E, De Angelis F, Grätzel M. A computational investigation of organic dyes for dye-sensitized solar cells: benchmark, strategies, and open issues. J Phys Chem C 2010;114:7205–12.

[4] (a) Selected examples: Zhang G-L, Bala H, Cheng Y-M, Shi D, Lv X-J, Yu Q-J, et al. High efficiency and stable dye-sensitized solar cells with an organic chromophore featuring a binary π-conjugated spacer Chem Commun; 2009:2198–200;
(b) Li Q-Q, Lu L-L, Zhong C, Huang J, Huang Q, Shi J, et al. New pyrrole-based organic dyes for dye-sensitized solar cells: convenient syntheses and high efficiency. Chem Eur J 2009;15:9664–8;
(c) Choi H, Kang SO, Ko J, Gao G, Kang HS, Kang M-S, et al. An efficient dye-sensitized solar cell with an organic sensitizer encapsulated in a cyclodextrin cavity. Angew Chem Int Ed 2009;48:5938–41;
(d) Im H, Kim S, Park C, Jang S-H, Kim C-J, Kim K, et al. High performance organic photosensitizers for dye-sensitized solar cells. Chem Commun 2010;46:1335–7;
(e) Choi H, Raabe I, Kim D, Teocoli F, Kim C, Song K, et al. High molar extinction coefficient organic sensitizers for efficient dye-sensitized solar cells. Chem Eur J 2010;16:1193–201;
(f) Chen C-H, Hsu Y-C, Chou H-H, Thomas KRJ, Lin JT, Hsu CP. Dipolar compounds containing fluorene and a heteroaromatic ring as the conjugating bridge for high-performance dye-sensitized solar cells. Chem Eur J 2010;16:3184–93;
(g) Liu X-Z, Zhang W, Uchida S, Cai L-P, Liu B, Ramakrishna S. An efficient organic-dye-sensitized solar cell with in situ polymerized poly(3,4-ethylenedioxythiophene) as a hole-transporting material. Adv Mater 2010;22: E150–5.

[5] (a) Coe BJ, Harris JA, Asselberghs I, Clays K, Olbrechts G, Persoons A, et al. Quadratic nonlinear optical properties of *N*-aryl stilbazolium dyes. Adv Funct Mater 2002;12:110–6;
(b) Coe BJ, Harris JA, Asselberghs I, Wostyn K, Clays K, Persoons A, et al. Quadratic optical nonlinearities of *N*-methyl and *N*-aryl pyridinium salts. Adv Funct Mater 2003;13:347–57;
(c) Coe BJ, Foxon SP, Harper EC, Harris JA, Helliwell M, Raftery J, et al. The syntheses, structures and nonlinear optical and related properties of salts with julolidinyl electron donor groups. Dyes Pigments 2009;82:171–86.

[6] (a) Other recent examples: Coe BJ. Switchable nonlinear optical metallochromophores with pyridinium electron acceptor groups Acc Chem Res 2006;39:383–93;
(b) Kim HS, Sohn KW, Jeon Y, Min H, Kim D, Yoon KB. Aligned inclusion of *n*-propionic acid tethering hemicyanine into silica zeolite film for second harmonic generation. Adv Mater 2007;19:260–3;
(c) Figi H, Mutter L, Hunziker C, Jazbinšek M, Günter P, Coe BJ. Extremely large nonresonant second-order nonlinear optical response in crystals of the stilbazolium salt DAPSH. J Opt Soc Am B 2008;25:1786–93;
(d) Compain J-D, Mialane P, Dolbecq A, Marrot J, Proust A, Nakatani K, et al. Second-order nonlinear optical properties of polyoxometalate salts of a chiral stilbazolium derivative. Inorg Chem 2009;48:6222–8;
(e) Coe BJ, Fielden J, Foxon SP, Brunschwig BS, Asselberghs I, Clays K, et al. Combining very large quadratic and cubic nonlinear optical responses in extended, tris-chelate metallochromophores with six π-conjugated pyridinium substituents. J Am Chem Soc 2010;132:3496–513.

[7] (a) Selected examples: Kim Y-H, Das A, Zhang H-Y, Dutta PK. Zeolite membrane-based artificial photosynthetic assembly for long-lived charge separation J Phys Chem B 2005;109:6929–32;
(b) Lainé PP, Bedioui F, Loiseau F, Chiorboli C, Campagna S. Conformationally gated photoinduced processes within photosensitizer–acceptor dyads based on osmium(II) complexes with triarylpyridinio-functionalized terpyridyl

ligands: insights from experimental study. J Am Chem Soc 2006;128: 7510–21;
(c) Weber JM, Rawls MT, MacKenzie VJ, Limoges BR, Elliott CM. High energy and quantum efficiency in photoinduced charge separation. J Am Chem Soc 2007;129:313–20;
(d) Zhang H-Y, Rajesh CS, Dutta PK. Ruthenium polypyridyl complexes containing a conjugated ligand L_{DQ} (L_{DQ} = 1-[4-(4′-methyl)-2,2′-bipyridyl]-2-[4-(4′- *N*, *N*′-tetramethylene-2,2′-bipyridinum)]ethene): synthesis, characterization, and photoinduced electron transfer at solution-zeolite interfaces. J Phys Chem C 2009;113:4623–33.

[8] SAINT (Version 6.45) and SADABS (Version 2.10). Madison: Wisconsin, USA: Bruker AXS Inc; 2003.

[9] Sheldrick GM. Phase annealing in *SHELX*-90: direct methods for larger structures. Acta Crystallogr Sect A 1990;46:467–73.

[10] Sheldrick GM. SHELXL 97, Program for crystal structure refinement. Göttingen, Germany: University of Göttingen; 1997.

[11] SHELXTL (Version 6.10). Madison: Wisconsin, USA: Bruker AXS Inc; 2000.

[12] Becke AD. Density-functional thermochemistry. III. The role of exact exchange. J Chem Phys 1993;98:5648–52.

[13] Krishnan R, Binkley JS, Seeger R, Pople JA. Self-consistent molecular orbital methods. XX. A basis set for correlated wave functions. J Chem Phys 1980;72: 650–4.

[14] Frisch MJ, Trucks GW, Schlegel HB, Scuseria GE, Robb MA, Cheeseman VG, et al. Gaussian 03, Revision C.02. Wallingford CT: Gaussian, Inc.; 2004.

[15] (a) Barone V, Cossi M. Quantum calculation of molecular energies and energy gradients in solution by a conductor solvent model. J Phys Chem A 1998;102: 1995–2001;
(b) Cossi M, Rega N, Scalmani G, Barone V. Energies, structures, and electronic properties of molecules in solution with the C-PCM solvation model. J Comp Chem 2003;24:669–81.

[16] O'Boyle NM, Tenderholt AL, Langner KM. cclib: a library for package-independent computational chemistry algorithms. J Comp Chem 2008;29:839–45.

[17] Kwon O, Barlow S, Odom SA, Beverina L, Thompson NJ, Zojer E, et al. Aromatic amines: a comparison of electron-donor strengths. J Phys Chem A 2005;109: 9346–52.

[18] Liu Y-L, Feng J-K, Ren A-M. Theoretical study of optical and electronic properties of the bis-dipolar diphenylamino-endcapped oligoarylfluorenes as promising light emitting materials. J Phys Org Chem 2007;20:600–9.

[19] Peter LM. Dye-sensitized nanocrystalline solar cells. Phys Chem Chem Phys 2007;9:2630–42.

[20] Kalyanasundranam K, editor. Dye sensitized solar cells. Lausanne, Switzerland: EPFL Press; 2010.

[21] Wang HX, Peter LM. A comparison of different methods to determine the electron diffusion length in dye-sensitized solar cells. J Phys Chem C 2009; 113:18125–33.

[22] Park N-G, Chang S-H, van de Lagemaat J, Kim K-J, Frank AJ. Effect of cations on the open-circuit photovoltage and the charge-injection efficiency of dye-sensitized nanocrystalline rutile TiO_2 films. Bull Korean Chem Soc 2000;21: 985–8.

[23] Lemon BI, Liu F, Hupp JT. Electrochemical, spectral, and quartz crystal microgravimetric assessment of conduction band edge energies for nanocrystalline zirconium dioxide/solution interfaces. Coord Chem Rev 2004;248: 1225–30.

[24] (a) Kusama H, Orita H, Sugihara H. DFT investigation of the TiO_2 band shift by nitrogen-containing heterocycle adsorption and implications on dye-sensitized solar cell performance. Sol Energ Mat Sol Cells 2008;92: 84–7;
(b) De Angelis F, Fantacci S, Selloni A. Alignment of the dye's molecular levels with the TiO_2 band edges in dye-sensitized solar cells: a DFT–TDDFT study. Nanotechnology 2008;19:424002.

[25] Keis K, Lindgren J, Lindquist S-E, Hagfeldt A. Studies of the adsorption process of Ru complexes in nanoporous ZnO electrodes. Langmuir 2000;16: 4688–94.

[26] (a) Onwona-Agyeman B, Kaneko S, Kumara A, Okuya M, Murakami K, Konno A, et al. Sensitization of nanocrystalline SnO_2 films with indoline dyes. Jpn J Appl Phys, Part 2 2005;44:L731–3;
(b) Minoura H, Yoshida T. Electrodeposition of ZnO/dye hybrid thin films for dye-sensitized solar cells. Electrochemistry 2008;76:109–17;
(c) Guillén E, Idígoras J, Berger T, Anta JA, Fernández-Lorenzo C, Alcántara R, et al. ZnO-based dye solar cell with pure ionic-liquid electrolyte and organic sensitizer: the relevance of the dye-oxide interaction in an ionic-liquid medium. Phys Chem Chem Phys 2011;13:207–13.

[27] (a) Nozik A. Photochemistry: applications to solar energy conversion. Annu Rev Phys Chem 1978;29:189–222;
(b) Serpone N, Pelizzetti E, editors. Photocatalysis: fundamentals and applications. New York: Wiley; 1989.